

# Analyzing Machupo virus-receptor binding by molecular dynamics simulations

Austin G. Meyer<sup>1,2,3\*</sup>, Sara L. Sawyer<sup>2</sup>, Andrew D. Ellington<sup>2</sup>,  
and Claus O. Wilke<sup>1</sup>

Address:

<sup>1</sup>Department of Integrative Biology, Institute for Cellular and Molecular Biology, and Center for Computational Biology and Bioinformatics. The University of Texas at Austin, Austin, TX 78712, USA.

<sup>2</sup>Department of Molecular Biosciences, Institute for Cellular and Molecular Biology, The University of Texas at Austin, Austin, TX 78712, USA.

<sup>3</sup>School of Medicine, Texas Tech University Health Sciences Center, Lubbock, TX 79430, USA.

\*Corresponding author

Email: austin.meyer@utexas.edu

Phone: +1 512 971 0123

Manuscript type: research article

Keywords: protein–protein interaction, molecular dynamics, arenavirus, machupo

## Abstract

In many biological applications, we would like to be able to computationally predict mutational effects on affinity in protein-protein interactions. However, many commonly used methods to predict these effects perform poorly in important test cases. In particular, the effects of multiple mutations, nonalanine substitutions, and flexible loops are difficult to predict with available tools and protocols. We present here an existing method applied in a novel way to a new test case; we interrogate affinity differences resulting from mutations in a host-virus protein-protein interface. We use steered molecular dynamics (SMD) to computationally pull the machupo virus (MACV) spike glycoprotein (GP1) away from the human transferrin receptor (hTfR1). We then approximate affinity using the maximum applied force of separation and the area under the force-versus-distance curve. We find, even without the rigor and planning required for free energy calculations, that these quantities can provide novel biophysical insight into the GP1/hTfR1 interaction. First, with no prior knowledge of the system we can differentiate among wild type and mutant complexes. Moreover, we show that this simple SMD scheme correlates well with relative free energy differences computed via free energy perturbation. Second, although the static co-crystal structure shows two large hydrogen-bonding networks in the GP1/hTfR1 interface, our simulations indicate that one of them may not be important for tight binding. Third, one viral site known to be critical for infection may mark an important evolutionary suppressor site for infection-resistant hTfR1 mutants. Finally, our approach provides a framework to compare the effects of multiple mutations, individually and jointly, on protein-protein interactions.

## 22 1 Introduction

23 The computational prediction of mutational effects on protein–protein interactions remains a chal-  
24 lenging problem. Several methods are available to perform an energy difference calculation from an  
25 experimentally determined co-crystal structure. For example, end point methods can be performed  
26 rapidly, with relatively low computational cost (Gront et al. 2011; Kortemme et al. 2004). How-  
27 ever, such methods can suffer from various simplifying assumptions. For example, they generally  
28 use an implicit solvent approximation and assume the end state difference with minimal structural  
29 rearrangement is sufficient to discriminate energetic differences (Gront et al. 2011; Kortemme et al.  
30 2004). Alternative approaches have been developed using machine learning, training coefficients  
31 in a weighted equation containing geometric and energetic parameters (Vreven et al. 2011, 2012;  
32 Bajaj et al. 2011; Hwang et al. 2010). Unfortunately, such machine-learning approaches often suf-  
33 fer in novel applications, for which available training sets are small or non-existent. As such, these  
34 methods are poorly suited for most host-virus protein–protein systems. By contrast, first principles  
35 methods can forgo training, but currently available methods such as free energy perturbation (FEP)  
36 and thermodynamic integration (TI) rely on a transitional model (where one state may be wild-type  
37 and the other may be a mutant) to make rigorous free energy calculations (Gilson et al. 1997; Lu  
38 et al. 2004; Chodera et al. 2011; Gumbart et al. 2013a). While these may be considered two of the  
39 gold standard techniques for calculating affinity differences, there are a huge number of theoreti-  
40 cal and technical complexities that must all be properly managed to ensure a converged solution  
41 (Gumbart et al. 2013b). Such considerations quickly come to dominate the protocol, and the nec-  
42 essary book keeping introduces the possibility of human error (Gumbart et al. 2013b). Moreover,  
43 as the two ending states look ever more dissimilar the chances of convergence fall rapidly. To en-  
44 sure convergence, these techniques are typically limited to small differences (such as point mutant  
45 comparisons) with a few, very impressive exceptions (Wang et al. 2006; Gumbart et al. 2013a,b).  
46 For most investigators, larger differences quickly become intractable as the number of intermedi-  
47 ate steps required to compute a converged solution grows or the complexity of adding restraining  
48 potentials and computing approximations expands (Wang et al. 2006; Gumbart et al. 2013a,b).

49 Here we propose that much of these complexities can be avoided if all we are interested in is a  
50 relative comparison of the effects of different mutations on protein-protein interactions, rather than

51 measuring an absolute or relative binding affinity with experimentally realistic units. We impart  
52 a pulling force within an all-atom molecular dynamics simulation on one member of the complex  
53 while the other is held in place. Then, we measure the force required for dissociation (Lu and  
54 Schulten 1999; Isralewitz et al. 2001b,a; Park and Schulten 2004; Gumbart et al. 2012; Miño et al.  
55 2013). Although such biasing techniques are commonly used in protein-ligand binding problems,  
56 they are less commonly applied to protein–protein interactions, and almost never to mutational  
57 analysis in a protein–protein system. This is largely the result of free energy convergence dif-  
58 ficulties and computational limitations (Cuendet and Michelin 2008; Cuendet and Zoete 2011).  
59 Using a proxy for relative binding affinity rather than caluclating absolute affinities can solve these  
60 problems. Here, as proxies, we use the maximum applied force required for separation and the  
61 area under the force-versus-distance curve (AUC). For comparison, we also calculate relative free  
62 energy differences using the traditional dual topology FEP paradigm, and we show that the two  
63 approaches yield congruent results.

64 We used SMD and FEP to interrogate the interaction between machupo virus (MACV) spike  
65 glycoprotein (GP1) and the human transferrin receptor (hTfR1) (Abraham et al. 2010; Charrel and  
66 de Lamballerie 2003). Machupo virus is an ambisense RNA virus of the arenavirus family (Char-  
67 rel and de Lamballerie 2003). Worldwide, arenaviruses represent a significant source of emerging  
68 zoonotic diseases for the human population (Charrel and de Lamballerie 2003). Members of the  
69 arenavirus family include the Lassa fever virus endemic to West Africa, the lymphochoriomening-  
70 gitis virus (LCMV) endemic to rodents in several areas of the United States, and the Guanarito,  
71 Junin, and Machupo viruses endemic to rodents in South America (Charrel and de Lamballerie  
72 2003). The South American arenaviruses typically infect humans after rodent contamination and  
73 can cause a devastating hemorrhagic fever with high mortality (Charrel and de Lamballerie 2003).

74 The hTfR1 is the primary receptor used by MACV for binding its host cell prior to infection.  
75 The primary role of hTfR1 *in vivo* is to bind transferrin for cellular iron uptake. The hTfR1 protein  
76 contains three extracellular domains: two basilar domains and an apical domain. The two basilar  
77 domains serve most of the transferrin-binding function (Abraham et al. 2010; Radoshitsky et al.  
78 2011). Viral entry is initiated by GP1 binding to the apical domain of hTfR1. Previous work has  
79 indicated that the GP1/hTfR1 binding interaction is the primary determinant of MACV host range  
80 variation (Choe et al. 2011; Radoshitsky et al. 2011). The co-crystal structure shows that the high

81 affinity interaction between GP1 and hTfR1 forces the normally flexible loop in the apical domain  
82 of hTfR1 into a rigid  $\beta$ -pleated sheet domain. For GP1, several extended loops mediate binding to  
83 hTfR1 (Abraham et al. 2010; Radoshitzky et al. 2011), and many of the interface interactions are  
84 mediated by extensive hydrogen-bonding networks (Abraham et al. 2010). Experimental alanine-  
85 scanning and whole-cell infectivity assays have identified several sites in both GP1 and hTfR1 that  
86 are probably critical for establishing infection (Choe et al. 2011; Radoshitzky et al. 2011).

87 We applied our computational method to wild type (WT) and mutant complexes, and found  
88 that we could resolve relative differences in unbinding and predict significant affinity changes.  
89 Importantly, the affinity changes predicted using only max force or AUC show a strong correlation  
90 with rigorous relative free energy differences computed by FEP. At sites known to be important for  
91 successful viral entry, we found that the biochemical cause of reduced infectivity may not be as  
92 simple as the static structure suggests. For example, the static structure shows a hydrogen-bonding  
93 network connected to site N348 in hTfR1. According to our simulations, this network may not  
94 affect binding affinity directly. In addition, our study offers an all-atom steered molecular dynamic  
95 approach to avoid some of the pitfalls of several existing methods used to evaluate mutations in  
96 protein–protein interfaces.

## 97 2 Materials and Methods

### 98 2.1 System Modeling

99 For our experiments, we used the experimentally determined GP1/hTfR1 structure (PDB-ID: 3KAS)  
100 (Abraham et al. 2010). The apical domain of hTfR1 interacts directly with GP1 while the other two  
101 domains are closer to the cell membrane and have essentially no interaction with GP1. The bio-  
102 physical independence of the apical domain allowed us to isolate it without significantly affecting  
103 the GP1/hTfR1 interaction.

104 We used the protein visualization software PyMOL (Schrödinger 2010) to remove residues  
105 121-190, 301-329, and 383-756 in the hTfR1. No residues were removed from the viral protein.  
106 Figure 1 shows a model of the initial structure and that of the pared structure. Although GP1 has  
107 several glycosylatable residues, we opted to use the de-glycosylated protein for this study. The

108 complexity of correctly parameterizing diverse sugar moieties is outside of the scope of this paper.  
109 Furthermore, although it is known that GP1 is glycosylated, and some of those sugars contact  
110 hTfR1, the sugars in the available PDB structure are not physiological for mammals (Abraham  
111 et al. 2010). In total we removed 10 sugars from the crystal structure for this study.

112 After system reduction, the Visual Molecular Dynamics (VMD) (Humphrey et al. 1996) pack-  
113 age along with its system of back-ends was used for all subsequent modeling. The Orient add-on  
114 package allowed us to rotate the system axis such that the direction of steering was oriented di-  
115 rectly down the z-axis. De-glycosylation simplified the system such that Autopsf could easily find  
116 the chain terminations and patch them appropriately. The Solvate package was used to generate a  
117 TIP3P water model with a 5 Ångstrom buffer (relative to the maximum dimensions of the proteins)  
118 on all sides except down the positive z-axis where a 20 Ångstrom buffer was created. Finally, we  
119 used the Autoionize package to place 150 millimolar NaCl and neutralize the total system charge.  
120 In the end, each modeled system had approximately 28,000 atoms.

## 121 **2.2 Equilibration**

122 NAMD was used for all simulations in this study (Phillips et al. 2005). In addition to the modeled  
123 system, for equilibration we generated a configuration file that fixed the  $\alpha$ -carbon backbone. This  
124 was accomplished by setting the B-factor column to 1 for the fixed atoms and to zero for all other  
125 atoms. Further, we generated a configuration file with fixed  $\alpha$ -carbon atoms at residues 41-92 (num-  
126 bered linearly, in this case, starting at 1 for the first amino acid as was required for NAMD) in the  
127 hTfR1. The second file was used to affix a harmonic restraint, thus preventing any unfolding due to  
128 system reduction. More importantly, the harmonic restraint allowed the protein complex to equili-  
129 brate while preventing any drift from its predefined position; the restraint did not constrain the struc-  
130 ture of each protein, or the relative position or orientation of the two proteins to each other. Finally,  
131 we calculated the system center and dimensions for use in molecular dynamics settings. The exact  
132 NAMD configuration files are available on github ([https://github.com/clauswilke/MACV\\_SMD](https://github.com/clauswilke/MACV_SMD)).

133 We used the Charmm27 (Brooks et al. 1983) all-atom force field. The initial system temperature  
134 was set to 310K. Several typical MD settings were used including switching and cutoff distances  
135 (see provided configuration files). In addition, we used a 2 femtosecond time step with rigid bonds.  
136 We used periodic boundary conditions with the particle mesh ewald (PME) method of computing

137 full system electrostatics outside of the explicit box. Furthermore, we used a group pressure cell,  
138 flexible box, langevin barostat, and lavegin thermostat during equilibration. A harmonic restraint  
139 (called harmonic constraint in VMD) was set as stated previously.

140 To start the simulation, the barostat was switched off and the system was minimized for 1000  
141 steps. Next, the fixed backbone was released, and the system was minimized for an additional 1000  
142 time steps. Subsequently, the system was released into all-atom molecular dynamics for 3000 steps.  
143 Finally, the langevin barostat was turned on and the system was simulated for 2 ns (1,000,000 steps)  
144 of chemical time. For each mutant, twenty independent equilibration replicates were run with an  
145 identical protocol.

### 146 2.3 Steered Molecular Dynamics

147 We used the final state from each equilibrated system to restart another MD simulation. Our steer-  
148 ing protocol is fundamentally similar to Cuendet and Michelin (2008) with slightly different pa-  
149 rameter choices. Perhaps the one significant difference lies in our choosing to not use a thermostat  
150 or barostat. We can make this choice because we are not trying to calculate the binding free en-  
151 ergy by any physically rigorous approach (the Jarzynski inequality being one example). Following  
152 equilibration, the final state of each simulation was used to generate a configuration file fixing the  
153  $\alpha$ -carbon on residues 1, 58, 73-83, 96, 136, 137, 138, and 161 (again with linear numbering) in  
154 the hTfR1. These residues were selected as they are far from the binding interface and sufficiently  
155 distributed to prevent any orientational motion of the receptor relative to the viral spike protein.  
156 The center of mass of the  $\alpha$ -carbons of all residues (163-318 in linear numbering) in GP1 received  
157 an applied force during the simulation. The NAMD convention does not actually apply a force to  
158 all  $\alpha$ -carbon atoms but rather uses the selection to compute an initial center of mass. Then, during  
159 the steering run, the single center of mass point is pulled with the parameters described below.  
160 We used the same force field parameters (exclude, cutoff, switching, etc.), the same integrator pa-  
161 rameters (time step, rigidbonds on, all molecular being wrapped, etc.), and the same particle mesh  
162 ewald parameters as in equilibration. Periodic boundary conditions were incorporated as part of  
163 the system (as is the convention in NAMD restart) and PME was again used to approximate full  
164 system electrostatics.

165 We ran test simulations at several force constants and visually inspected the results. A force

constant of 5 kcal/mol/Å<sup>2</sup> was chosen due to its relatively low signal-to-noise ratio. This constant is slightly lower than the more common 7 kcal/mol/Å<sup>2</sup> found in several recent studies; that value is commonly selected primarily because it is the force constant found in the SMD tutorial available through the NAMD developers. Moreover, the force constant could very likely be set to a range of nearby values with little loss in predictive power.

In SMD experiments the pulling velocity should be as low as possible for the available computational time (Cuendet and Michielin 2008; Cuendet and Zoete 2011). We choose a velocity of 0.000001 Å/fs = 1 Å/ns, and direction down the positive *z*-axis. One could use faster pulling if the computing time must be reduced, but slower than necessary pulling speeds are not typically considered problematic.

SMD was run for 15 ns (7,500,000 time steps) of chemical time. For each simulation, we randomly selected one of the equilibration runs for restart. We ran 50 replicate simulations per mutant for a total of 550 SMD simulations. All GP1/hTfR1 complexes separated by greater than 4 Å and many separated to 10 or more.

To leave the final trajectory of a tractable size, only 1000 evenly spaced frames were retained from each simulation, leaving a final trajectory size of 323 MB. See the supplemental movie for a representative unbinding trajectory. Initial development of the SMD protocol was carried out on the Lonestar cluster at the Texas Advanced Computing Center (TACC). All production SMD simulations were performed on the Hrothgar cluster at Texas Tech University, using NAMD 2.9. Each simulation was parallelized over 60 computational cores and utilized approximately 20 hours of computing time. The total chemical time simulated for this project was nearly 10 μs, requiring slightly over 1 million cpu-hours.

## 2.4 Free Energy Perturbation

Briefly, we used the traditional dual topology approach to FEP (Gao et al. 1989; Pearlman 1989). This involves a thermodynamic cycle where a set of atoms are progressively decoupled from the environment while another set of atoms are progressively coupled. To compute the relative free energy difference requires knowing the free energy change when the transformation is carried out for the bound complex and the individual protein. Then, one can compute the relative free energy difference between a WT and mutant complex by taking the difference between the energy required

195 to decouple/couple the atoms in solution from the energy required to decouple/couple the atoms in  
196 the bound complex (Gao et al. 1989; Pearlman 1989).

197 Again, the NAMD configuration file is made available via github ([https://github.com/clauswilke/MACV\\_SMD](https://github.com/clauswilke/MACV_SMD))  
198 We used a similar configuration to that in equilibration. One significant difference was to make a  
199 cubic water box with a side length equal to the long axis of the complex plus a 10 Å buffer on either  
200 side, and simply restrict center of mass motion with the NAMD setting. This was done to avoid  
201 affecting the system energy while calculating free energy differences.

202 The transition protocol for bound and free protein systems were identical. They started with  
203 1000 steps of minimization and 250,000 steps of equilibration in the starting state for the forward  
204 and reverse directions. Phase transitions were carried out in steps of  $\lambda=0.05$ . Each transition  
205 was carried out for 250,000 steps. The first 100,000 steps after phase transition were reserved for  
206 equilibration and the final 150,000 steps were used for data collection.

207 The VMD mutator tool was used to generate the necessary topology file and the parseFEP tool  
208 (Liu et al. 2012) in VMD was used for subsequent analysis. We used it to perform error analysis  
209 and compute the Bennett acceptance ratio as the maximum likelihood free energy difference of the  
210 two states under consideration. Though the larger transitions presented difficulty in a small number  
211 of windows, forward and reverse hysteresis was generally in good agreement for all complexes.  
212 The double mutants were performed by first doing the Y211A mutation followed by the other of  
213 the two mutants. Then, the  $\Delta G$ 's were simply added together to get the total energetic difference.

## 214 **2.5 Post-processing**

215 The python packages MDAnalysis (Michaud-Agrawal et al. 2011) and ProDy (Bakan et al. 2011)  
216 were both used at various points in post-processing. The molecular trajectory (comprising the  
217 atomic coordinates per time) was parsed to compute the center-of-mass for each of the two com-  
218 plexes. The starting center-of-mass distance was set to zero and the distance was re-computed at  
219 each time step relative to the starting distance.

220 The statistical package R was used for all further analysis and visualization. Each of the 50  
221 independent trajectories per mutant produced a fairly noisy force curve. The force curves for each  
222 mutant were smoothed over all replicates by using the smooth.spline() and predict() functions in R  
223 with default settings. The two primary descriptive statistics we used were maximum interpolated

224 applied force and total area under the interpolated curve (AUC). We tested for significant differences  
225 in maximum force or AUC by carrying out t tests for all pairwise combinations (each mutant com-  
226 pared to each other mutant), using the pairwise.t.test() function in R. We adjusted p values to cor-  
227 rect for multiple testing using the False-Discovery-Rate (FDR) method (Benjamini and Hochberg  
228 1995). The ggplot (Wickham 2009) package was used to generate most of the figures.

229 Analysis scripts and final data (except MD trajectories) are available on the github repository  
230 accompanying this publication ([https://github.com/clauswilke/MACV\\_SMD](https://github.com/clauswilke/MACV_SMD)).

## 231 3 Results

### 232 3.1 The GP1/hTfR1 system

233 The GP1/hTfR1 interface (Figure 2) marks a particularly important and useful test system. There  
234 are several sites on both the human and viral protein known to affect the infectivity phenotype  
235 of MACV. Many of the important sites have been mapped by *in vitro* flow-cytometry based entry  
236 assays. The GP1/hTfR1 interface appears not to be dominated by one particular type of interaction  
237 (electrostatics, hydrogen-bonding, or van der Waals). In addition, much of the binding domain  
238 on hTfR1 is on a loop that is flexible prior to viral binding, but organizes to become a strand  
239 of a  $\beta$ -sheet on binding. As a result, many other computational techniques (Gront et al. 2011;  
240 Kortemme et al. 2004) are only marginally useful. The complex nature of this interface represents  
241 a particularly difficult challenge for traditional computational analysis.

242 In total, we tested 7 point mutants and 3 double mutants in addition to the WT complex (Ta-  
243 ble 1). All of the mutations are within 5 Å of the protein–protein interface. Mutations in hTfR1  
244 at site 211 have proven capable of causing loss-of-entry according to *in vitro* flow-cytometry in-  
245 fection assays or known host-range limitations (Radoshitzky et al. 2008; Choe et al. 2011; Ra-  
246 doshitzky et al. 2011). Most likely, this effect is caused by the destruction of a critical hydrogen  
247 bond to Ser113 or Ser111 in GP1. The lost hydrogen bond would lead to the subsequent loss of a  
248 large hydrogen-bonding network seen in the crystal structure (Table 1) (Abraham et al. 2010). In a  
249 manner similar to site 211, N348 appears to be important for binding by participating in a critical  
250 hydrogen bonding network (Radoshitzky et al. 2008; Abraham et al. 2010) to GP1. In particular,

251 N348Lys is reported in the literature to cause significantly reduced viral entry *in vivo* (Table 1)  
252 (Radoshitsky et al. 2008; Abraham et al. 2010). Finally, an alanine mutation at site 111 in GP1  
253 (mutation vR111A) has also been shown to cause decreased entry (Table 1) (Radoshitsky et al.  
254 2011). For notation purposes, the viral site is always referred to with a preceding ‘v’.

255 Despite the fact that viral binding occurs at the site of a flexible loop in the free hTfR structure,  
256 our data shows after binding the strand is extremely rigid. In the bound conformation, only two  
257 sites of the loop have root mean squared fluctuation (RMSF) values in the top half of all receptor  
258 sites during equilibration (Figure 3), and those are almost completely exposed to solvent. This is  
259 unsurprising considering the high degree of burial that occurs as a result of viral binding. Com-  
260 puting the root mean squared deviation (RMSD) of the entire structure over the trajectory shows  
261 that none of the mutations are so deleterious as to cause rapid unbinding. In fact, the RMSD over  
262 trajectory looks highly invariant across mutants (Figure 4). In the unbound state, calculated near  
263 the end of the SMD trajectory, all of the residues in the WT receptor interfacial strand are in the  
264 top half of RMSF over all receptor sites (Figure 5). Thus, if sufficient simulation time is not ded-  
265 icated to allowing this unfolding process, standard free energy techniques may miss the energetic  
266 contributions that result from ordering the flexible loop in the hTfR apical domain.

### 267 3.2 Molecular dynamics simulations

268 We analyzed the GP1/hTfR1 system using two molecular dynamics techniques. First, by carrying  
269 out SMD using a known force constant and pulling with a constant velocity, we could calculate  
270 the applied force during protein–protein dissociation (Cuendet and Michelin 2008; Cuendet and  
271 Zoete 2011). A typical averaged force curve comparison can be seen in Figure 6, and individual  
272 images of all averaged force curves are available in the associated github repository, in folder  
273 figures/force\_curves. As seen in Figure 6, the dissociation distance was relatively consistent among  
274 mutants. The supplementary movie visually illustrates the separation distance between peptide  
275 domains. The quantities maximum applied force and AUC were derived from the force-versus-  
276 distances curves. Their summary statistics are reported in Table 2. As we are more interested in  
277 the phenotypic impact of interface mutations we avoided many of the more physically rigorous, but  
278 technically complicated calculations that are possible with SMD (Isralewitz et al. 2001b,a).

279 Before systematically applying SMD to the GP1/hTfR1 interaction, we needed to ensure the

method was sufficiently sensitive to distinguish between relatively minor point mutations. While SMD has been applied previously to measure the binding energy of high-affinity T-cell receptor interactions (Cuendet and Michelin 2008; Cuendet and Zoete 2011), it is rarely used to parse small energy differences in a protein–protein interaction energy landscape. For this initial sensitivity analysis, we tested alanine substitutions congruent with the traditional experimental and computational approach.

We proceeded to compare our SMD results to that of the standard dual topology FEP approach to calculate relative free energy differences. The correlation between the energetically rigorous FEP and our statistical approach is high. For all 11 complexes tested, the correlation between max force and FEP was  $r = -0.795$  at  $p = 0.0034$  (Figure 7), and the correlation between AUC and FEP was  $r = -0.593$  at  $p = 0.055$ . Because of the strong correlation, we refer exclusively to the SMD results for the remainder of this work, focusing primarily on max force.

We found that relative to WT, one alanine mutation (Y211A) produced a very large and statistically significant difference in the maximum applied force and AUC (Figure 6, Table 3), while the other two did not (Table 3). When considering additional mutants (also discussed below), we found that maximum applied force was generally sufficient to distinguish mutants (Tables 3 and 4), and AUC was able to add a few more statistically significant differences (Table 5). In general, however, and consistent with the FEP results, maximum applied force seemed to be the more sensitive statistic than AUC.

### 3.3 Comparative analysis of the GP1/hTfR1 interface

Considering the involvement of extended hydrogen-bonding networks in the GP1/hTfR1 interface (Figure 2), it was not clear that individual alanine mutations, even those that should destroy such networks, would significantly change the strength of interaction. One major advantage of first principles simulations is the ability to test mutations other than alanine without additional underlying assumptions in the energy function. As shown in Table 1, we made additional mutations based on biochemical intuition or available experimental data to chemically diverse amino acids including tryptophan, lysine, aspartate, and threonine. Several mutations caused significant relative affinity changes. In addition, to detect synergistic effects, we tested several double mutants where both mutations appeared to cause similar changes in binding. Then, we compared the size of those

309 differences to single mutants (Figure 8 and 9).

310        Although Y211A appears to have a large impact on binding affinity, no single mutant can pro-  
311 vide enough evidence to understand the biochemical difference in binding mechanism. Since ala-  
312 nine is both smaller than tyrosine and also incapable of participating in hydrogen-bond interactions,  
313 we tested further mutations to identify the critical biochemical difference responsible for change in  
314 binding affinity. In particular, we substituted smaller side chains that, like tyrosine, were capable  
315 of hydrogen bonding. We chose Y211D and Y211T, two mutations that have been discussed in the  
316 context of selection pressure on hosts in rodent populations (Radoshitzky et al. 2008; Choe et al.  
317 2011; Radoshitzky et al. 2011). Both mutations proved capable of causing a significant change  
318 in binding affinity in our simulations, but the change appeared to be increased affinity (Figures 8  
319 and 9, and Table 4).

320        We also simulated several point mutations at N348 in the hTfR1. As discussed above, the  
321 alanine mutation at this site showed no significant difference in maximum applied force or AUC  
322 from WT (Tables 4 and 5). In addition, neither the N348Lys nor the N348W mutation showed  
323 a significant difference from WT. For both of these mutations, however, mean maximum applied  
324 force and mean AUC was lower than for WT (See Table 2). On the other hand, there was a de-  
325 tectable difference between N348A and N348Lys (Tables 4 and 5), with N348Lys being a weaker  
326 binder. Moreover, N348W showed nearly identical results to N348Lys. The mutations to large  
327 amino acids (N348W and N348Lys) produced nearly identical affinity changes, whereas the muta-  
328 tions to amino acids not capable of hydrogen bonding (N348A and N348W) produced significantly  
329 different affinity changes (Table 3). To check the consistency of our results, we hypothesized that  
330 the combination of Y211A and N348W, being chemically disconnected in two different hydrogen-  
331 bonding networks, would lead to a synergistic loss-of-binding. As expected, the double mutant  
332 was the weakest binding mutant tested ( $p < 10^{-6}$ , Tables 4 and 5) in this study. Further, according  
333 to maximum applied force (but not AUC), the combination of Y211A and N348W also showed  
334 significantly weaker binding than Y211A by itself (Tables 4 and 5). We suspect that the effect  
335 of N348W alone is near the limit of detection using our method. A larger number of replicates  
336 would possibly have resolved affinity differences between N348W and WT or other mutants more  
337 consistently.

338        Last, we further analyzed a single mutation in GP1, vR111A. As mentioned previously, in our

339 simulations this mutant showed no significant change in either maximum applied force or AUC  
340 (Tables 4 and 5), even though both quantities were, on average, lower than in WT (Table 2). This  
341 result was somewhat surprising, since Y211A, presumably disrupting the same hydrogen-bonding  
342 network as vR111A, displayed a significant reduction in affinity. To probe the interaction between  
343 position 111 in the GP1 and position 211 in the hTfR1 further, we also tested the double mutant  
344 vR111A/Y211A. This double mutant showed affinity indistinguishable from WT and significantly  
345 higher than Y211A alone (Table 3). This result shows that the two sites do indeed interact, and that  
346 replacing the hydrogen-bonding network at these sites with a hydrophobic interaction could lead to  
347 comparable binding affinity.

## 348 4 Discussion

349 We have applied a method utilizing steering forces in all-atom molecular dynamics simulations to  
350 evaluate the effects of mutations at the GP1/hTfR1 interface. We modeled mutations at several sites  
351 in the GP1/hTfR1 interface, and verified that our computational protocol was sensitive enough to  
352 distinguish point mutants in hTfR1. Further, we identified two test statistics, maximum applied  
353 force and AUC, that can be used as proxies for binding affinity. Both of these statistics correlate  
354 well with FEP, but offer the simplicity of not requiring a large commitment to planning for the  
355 theoretical issues inherent to free energy methods. We systematically tested several point mutations  
356 to understand their contribution to the binding interaction. In the case of N348Lys, we have shown  
357 that the static structure provides little insight into why this mutation causes loss-of-infectivity *in*  
358 *vivo*. While N348 appears to be involved in a hydrogen-bonding network in the static structure,  
359 change in binding at that site may actually be caused by size and charge restriction. We also found  
360 that a negatively polar residue at site 211 in hTfR1 seem critical for a tight binding interaction.  
361 Any non-polar mutation at Y211 in hTfR1 is likely to completely halt viral entry and dramatically  
362 decrease the chances of MACV infection.

363 Traditionally SMD has been either applied to compute equilibrium free energies via a non-  
364 equilibrium approximation (Park et al. 2003; Park and Schulten 2004; Giorgino and Fabritiis 2011),  
365 used to estimate protein stability through unfolding (Lu and Schulten 1999), or used to calculate the  
366 absolute free energy of small molecule ligand binding (Dixit and Chipot 2001). Likewise, others

367 have used SMD to understand the process of binding and unbinding at a resolution unmatched by  
368 experiment (Cuendet and Zoete 2011; Giorgino and Fabritiis 2011). Here, we have shown that  
369 SMD can provide insight into the *relative* strength of protein–protein interactions. Via SMD, one  
370 can separate mutations whose likely effect is altered binding affinity with simple statistics like  
371 maximum force of separation. Thus, SMD may open avenues for subsequent experimental work in  
372 some situations where FEP may be prohibitively difficult.

373 Our findings rationalize several effects observed in both infectivity data and rodent populations  
374 (Radoshitzky et al. 2008; Choe et al. 2011). First, we found that some substitutions at positions  
375 211 and 348 did affect the strength of receptor binding. However, the computational data suggest  
376 that the reason and nature of the effects at these two sites are very different. At position 211,  
377 mutations to non-polar residues cause a large change in binding. This is congruent with what is  
378 known from viral entry data (Radoshitzky et al. 2008; Choe et al. 2011). By contrast, mutations at  
379 position 348 need only be small to maintain WT binding. The ability to hydrogen bond appears to  
380 be insignificant. This can be inferred from the fact that Y211A paired with large (W) and positively  
381 charged (Lys) substitutions at position 348 results in a larger than expected synergistic difference.  
382 That is, the double mutant Y211A/N348W caused a much larger decrease in binding than we  
383 expected from either mutation individually. Third, the GP1 mutation vR111A causes a loss-of-  
384 infection during *in vitro* infectivity assays (Radoshitzky et al. 2011), yet it was indistinguishable  
385 from the WT complex in our simulations. Although Y211A was the most disruptive single mutant  
386 we tested, vR111A in the GP1 was able to restore mean maximum applied force to WT levels  
387 (Table 2), and to levels significantly higher than observed for Y211A alone.

388 We would like to emphasize here that we cannot expect perfect agreement between our simula-  
389 tions and the available experimental data, but the correspondence to a well established free energy  
390 method bolsters our conclusions. While we have shown that our method can distinguish individual  
391 point mutations, we do not know the limit of detection with our method. First, it is possible that  
392 some mutants display measurable phenotypic effects in experiments yet appear identical in simula-  
393 tion. More extensive sampling or refinement of the simulation protocol could help to differentiate  
394 such mutants (see also next paragraph). Second, the SMD method is fundamentally limited by the  
395 accuracy of our starting structure. Third, the available experimental data for the GP1/hTfR1 sys-  
396 tem were generally obtained from entry assays or whole-cell binding assays rather than molecular

397 binding assays. A mutant may cause a phenotypic difference in infectivity without generating a  
398 signal by our method. For example, entry could be lost in the experimental system because the  
399 protein is grossly or partially misfolded. An additional analytical step with circular dichroism or an  
400 analogous technique could clarify such large-scale folding differences. Further, since our simula-  
401 tions start with a bound structure, any changes that may dramatically affect the rate of association  
402 (different folds, trafficking issues, etc.) or relative orientation of the two proteins would be under-  
403 estimated by our method.

404 There are a few additional challenges for investigating host-virus interactions via molecular  
405 dynamics simulation. As with any atomistic simulation, there is going to be a fairly large noise-to-  
406 signal ratio. To reduce noise, one could further customize each simulation, e.g. by determining the  
407 optimal pulling speed. Furthermore, larger amounts of computational resources will have a direct  
408 and powerful impact on the strength of any atomistic study (Jensen et al. 2012). Such resources  
409 could come in the form of increased compute time, improved code, or customized hardware for  
410 floating point operations (Shaw et al. 2011). With improved resources, we could investigate thou-  
411 sands of individual permutations in the GP1/hTfR1 binding interface. In addition, with additional  
412 compute time it would be possible to incorporate equilibrium sampling approaches (Buch et al.  
413 2011) or use brute force equilibrium approaches (Giorgino et al. 2012) to improve resolution.

414 For future studies, although our approach offers the simplicity of not requiring prior knowledge  
415 about a system of interest (other than a bound model), at this point SMD may not be the best approach  
416 for many relative affinity calculations. To ensure one's results are independent of the dissociation  
417 path one selects would require computing the work of separation for all likely paths. Such an  
418 approach eventually requires using the Jarzynski inequality (Jarzynski 1997) to establish a lower  
419 limit for binding energy and would quickly become computationally inefficient for evaluating a  
420 large number of mutations in most systems. However, considering the strong correlation between  
421 FEP and SMD in this system, it may not be important to ensure one's results are path independent  
422 for relative affinity calculations, as long as the same path is used for all complexes.

423 More importantly, with no *a priori* knowledge of the appropriate number of equilibration sam-  
424 ples, the best duration of equilibration, the appropriate number of pulling runs, or the best pulling  
425 speed means the computational expense in our SMD protocol may not be commensurate with the  
426 information provided. For example, another all atom approach that makes calculations via short

427 simulations of spatially restrained complexes has proven capable of generating relatively accurate  
428 binding affinities with less compute time than is required from our steering strategy (Gumbart et al.  
429 2013a,b). That being said, there is no reason to believe this SMD approach to mutagenic stud-  
430 ies could not be optimized to reduce computational expense. Further analysis will be needed to  
431 understand the lower limits of resources required for accurate predictions.

## 432 5 Acknowledgements

433 This work was carried out using high-performance computing resources provided by the High Per-  
434 formance Computing Center (HPCC) at Texas Tech University at Lubbock (<http://www.hpcc.ttu.edu>)  
435 and the Texas Advanced Computing Center (TACC) at The University of Texas at Austin (<http://www.tacc.utexas.edu>).  
436 We would like to thank Bryan Sutton for opening access to the Hrothgar cluster and the reviewers  
437 Ilan Samish and Matteo Masetti for their helpful comments on this work.

## 438 References

- 439 **Abraham J, Corbett K, Farzan M, Choe H, Harrison S. 2010.** Structural basis for receptor  
440 recognition by new world hemorrhagic fever arenaviruses. *Nat. Struct. Mol. Bio.* **17**:438–444.
- 441 **Bajaj C, Chowdhury R, Siddhanavalli V. 2011.** *F<sup>2</sup>Dock*: Fast fourier protein-protein docking.  
442 *IEEE Transactions on Computational Biology and Bioinformatics* **8**:45–58.
- 443 **Bakan A, Meireles L, Bahar I. 2011.** ProDy: Protein dynamics inferred from theory and experi-  
444 ments. *Bioinformatics* **27**:1575–1577.
- 445 **Benjamini Y, Hochberg Y. 1995.** Controlling the false discovery rate: a practical and powerful  
446 approach to multiple testing. *J. Royal Stat. Soc., Series B* **57**:289–300.
- 447 **Brooks B, Bruccoleri R, Olafson B, States D, Swaminathan S, Karplus M. 1983.** CHARMM:  
448 A program for macromolecular energy, minimization, and dynamics calculations. *J. Comput.*  
449 *Chem.* **4**:187–217.

- 450 **Buch I, Sadiq S, Fabritiis GD.** 2011. Optimized potential of mean force calculations for standard  
451 binding free energies. *J. Chem. Theory Comput.* **7**:1765–1772.
- 452 **Charrel RN, de Lamballerie X.** 2003. Arenaviruses other than Lassa virus. *Antiviral Res.* **57**:89–  
453 100.
- 454 **Chodera J, Mobley D, Shirts M, Dixon R, Branson K, Pande V.** 2011. Alchemical free energy  
455 methods for drug discovery: progress and challenges. *Current Opinion in Structural Biology*  
456 **21**:150–160.
- 457 **Choe H, Jemielity S, Abraham J, Radoshitzky S, Farzan M.** 2011. Transferrin receptor 1 in the  
458 zoonosis and pathogenesis of new world hemorrhagic fever arenaviruses. *Current Opinion in*  
459 *Microbiology* **12**:467–482.
- 460 **Cuendet M, Michelin O.** 2008. Protein-protein interaction investigated by steered molecular  
461 dynamics: The TCR-PMHC complex. *Biophysical J.* **95**:3575–3590.
- 462 **Cuendet M, Zoete V.** 2011. How T-cell receptors interact with peptide-MHCs: A multiple steered  
463 molecular dynamics study. *Proteins* **79**:3007–3024.
- 464 **Dixit S, Chipot C.** 2001. Can absolute free energies of association be estimated from molecular  
465 mechanical simulations? The biotin-streptavidin system revisited. *J. Phys. Chem. A* **105**:9795–  
466 9799.
- 467 **Gao J, Kuczera K, Tidor B, Karplus M.** 1989. Hidden thermodynamics of mutant proteins: A  
468 molecular dynamics analysis. *Science* **244**:1069–1072.
- 469 **Gilson MK, Given JA, Bush BL, McCammon JA.** 1997. The statistical-thermodynamic basis for  
470 computation of binding affinities: A critical review. *Biophys. J* **72**:11047–1069.
- 471 **Giorgino T, Buch I, Fabritiis GD.** 2012. Visualizing the induced binding of SH2-phosphopeptide.  
472 *J. Chem. Theory Comput.* **8**:1171–1175.
- 473 **Giorgino T, Fabritiis GD.** 2011. A high-throughput steered molecular dynamics study on the free  
474 energy profile of ion permeation through Gramicidin A. *J. Chem. Theory Comput.* **7**:1943–1950.

- 475 **Gront D, Kulp DW, Vernon RM, Strauss CEM, Baker D.** 2011. Generalized fragment picking  
476 in Rosetta: Design, protocols and applications. *PLoS ONE* **6**.
- 477 **Gumbart J, Roux B, Chipot C.** 2013a. Standard binding free energies from computer simulations:  
478 What is the best strategy? *J. Chem. Theory Comput.* **9**:794–802.
- 479 **Gumbart J, Schreiner E, Wilson D, Beckmann R, Schulten K.** 2012. Mechanisms of SecM-  
480 mediated stalling in the ribosome. *Biophys. J.* **203**:331–341.
- 481 **Gumbart JC, Roux B, Chipot C.** 2013b. Efficient determination of protein-protein standard  
482 binding free energies from first principles. *J. Chem. Theory Comput.* **9**:3780–3798.
- 483 **Humphrey W, Dalke A, Schulten K.** 1996. VMD - Visual Molecular Dynamics. *J. Molec.*  
484 *Graphics* **14**:33–38.
- 485 **Hwang H, Vreven T, Janin J, Weng Z.** 2010. Protein-protein docking benchmark version 4.0.  
486 *Proteins* **78**:3111–3114.
- 487 **Isralewitz B, Baudrya J, Gullingsruda J, Kosztinav D, Schulten K.** 2001a. Steered molecular  
488 dynamics investigations of protein function. *J. Molec. Graphics* **19**:13–25.
- 489 **Isralewitz B, Gao M, Schulten K.** 2001b. Steered molecular dynamics and mechanical functions  
490 of proteins. *Current Opinion in Structural Biology* **25**:225–230.
- 491 **Jarzynski C.** 1997. Equilibrium free-energy differences from nonequilibrium measurements: A  
492 master-equation approach. *Physical Review E* **56**:5018–5035.
- 493 **Jensen M, Jogini V, Borhani D, Leffler A, Dror R, Shaw D.** 2012. Mechanism of voltage gating  
494 in potassium channels. *Science* **336**:229–233.
- 495 **Kortemme T, Kim DE, Baker D.** 2004. Computational alanine scanning of protein-protein inter-  
496 faces. *Sci. STKE* **2004**:12.
- 497 **Liu P, Dehez F, Cai W, Chipot C.** 2012. A toolkit for the analysis of free-energy perturbation  
498 calculations. *J. Chem. Theor. Comput.* **8**:2606–2616.

- 499 **Lu H, Schulten K. 1999.** Steered molecular dynamics simulations of force-induced protein domain  
500 unfolding. *Protein Struct. Funct. Genet.* **35**:453–463.
- 501 **Lu N, Kofke DA, Woolf TB. 2004.** Improving the efficiency and reliability of free energy pertur-  
502 bation calculations using overlap sampling methods. *J. Comput. Chem.* **25**:28–39.
- 503 **Miño G, Baez M, Gutierrez G. 2013.** Effect of mutation at the interface of Trp-repressor dimeric  
504 protein: a steered molecular dynamics simulation. *Eur. Biophys. J.* **42**:683–690.
- 505 **Michaud-Agrawal N, Denning E, Woolf T, Beckstein O. 2011.** MDAnalysis: A toolkit for the  
506 analysis of molecular dynamics simulations. *J. Comput. Chem.* **32**:2319–2327.
- 507 **Park S, Khalili-Araghi F, Tajkhorshid E, Schulten K. 2003.** Free energy calculation from steered  
508 molecular dynamics simulations using Jarzynski’s equality. *J. Chem. Phys.* **119**:3559–3567.
- 509 **Park S, Schulten K. 2004.** Calculating potentials of mean force from steered molecular dynamics  
510 simulations. *J. Chem. Phys.* **120**:5946–5961.
- 511 **Pearlman DA. 1989.** A comparison of alternative approaches to free energy calculations. *J. Phys.*  
512 *Chem.* **98**:1487–1493.
- 513 **Phillips J, Braun R, Wang W, Gumbart J, Tajkhorshid E, Villa E, Chipot C, Skeel R, Kale L,**  
514 **Schulten K. 2005.** Scalable molecular dynamics with NAMD. *J. Comput. Chem.* **26**:1781–1802.
- 515 **Radoshitsky S, Kuhn J, Spiropoulou C, Albarino C, Nguyen D, Salazar-Bravo J, Dorfman  
516 T, Lee A, Wang E, Ross S, Choe H, Farzan M. 2008.** Receptor determinants of zoonotic  
517 transmission of new world hemorrhagic fever arenaviruses. *Proc. Natl. Acad. Sci.* **19**:2664–  
518 2669.
- 519 **Radoshitsky S, Longobardi L, Kuhn J, Retterer C, Clester J, K Kota JC, Bavari S. 2011.**  
520 Machupo virus glycoprotein determinants for human transferrin receptor 1 binding and cell entry.  
521 *PLoS ONE* **6**.
- 522 **Schrödinger. 2010.** The PyMOL molecular graphics system, version 1.3r1. Schrödinger, LLC.

- 523 Shaw D, Dror R, Salmon J, Grossman J, Mackenzie K, Bank J, Young C, Deneroff M, Batson  
524 B, Bowers K, Chow E, Eastwood M, Ierardi D, Klepeis J, Kuskin J, Larson R, Lindorff-  
525 Larsen K, Maragakis P, Moraes M, Piana S, Shan Y, Towles B. 2011. Millisecond-scale  
526 molecular dynamics simulations on anton. *Proceedings of the Conference on High Performance*  
527 *Computing, Networking, Storage and Analysis* SC09:39.
- 528 Vreven T, Hwang H, Pierce B, Weng Z. 2012. Prediction of protein-protein binding free energies.  
529 *Protein Science* 21:396–404.
- 530 Vreven T, Hwang H, Weng Z. 2011. Integrating atom-based and residue-based scoring functions  
531 for protein-protein docking. *Protein Science* 20:1576–1586.
- 532 Wang J, Deng Y, Roux B. 2006. Absolute binding free energy calculations using molecular dy-  
533 namics simulations with restraining potentials. *Biophys. J.* 91:2798–2814.
- 534 Wickham H. 2009. *ggplot2: Elegant graphics for data analysis.* Springer New York. URL  
535 <http://had.co.nz/ggplot2/book>.

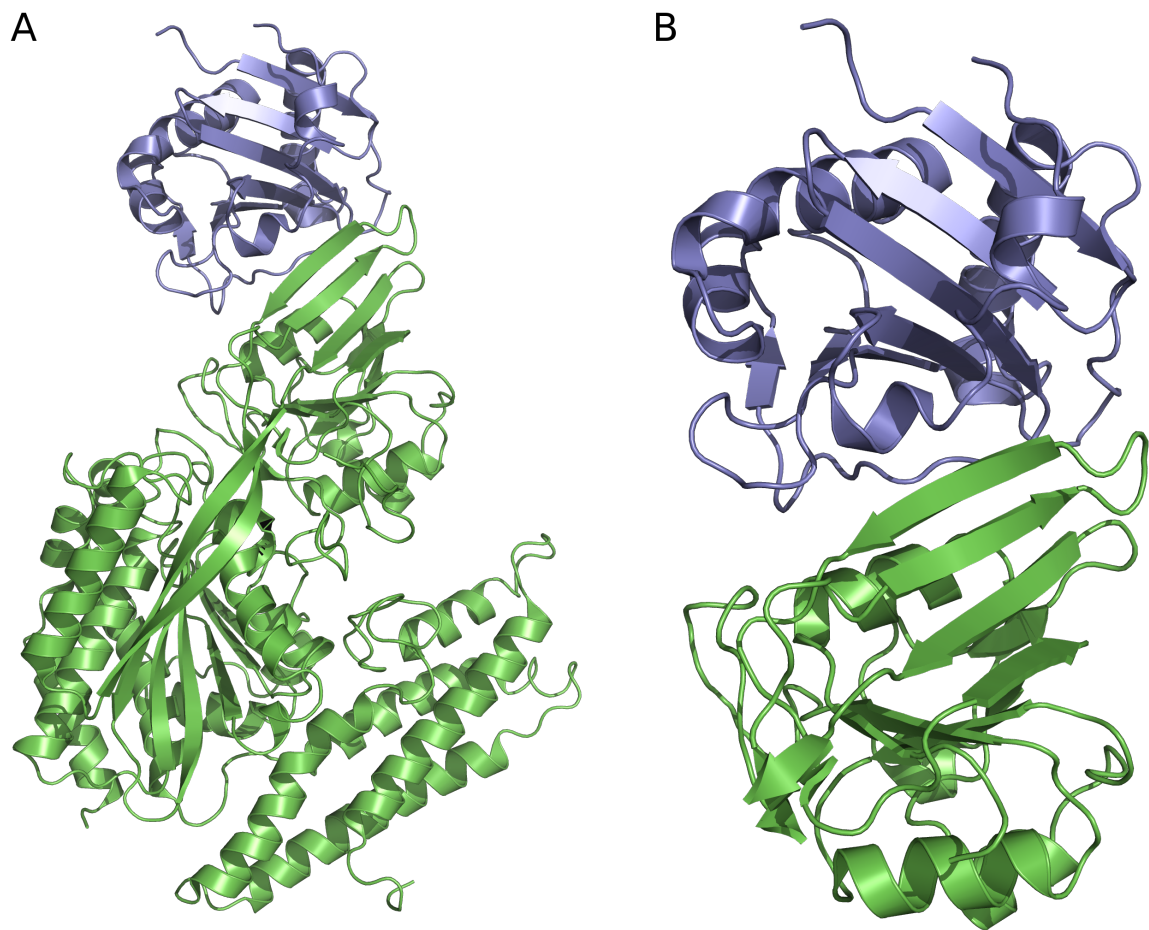


Figure 1: The GP1/hTfR1 complex. GP1 is shown in blue and hTfR1 is shown in green. (A) The full, de-glycosylated GP1/hTfR1 co-crystal structure. (B) The reduced structure used in SMD simulations.

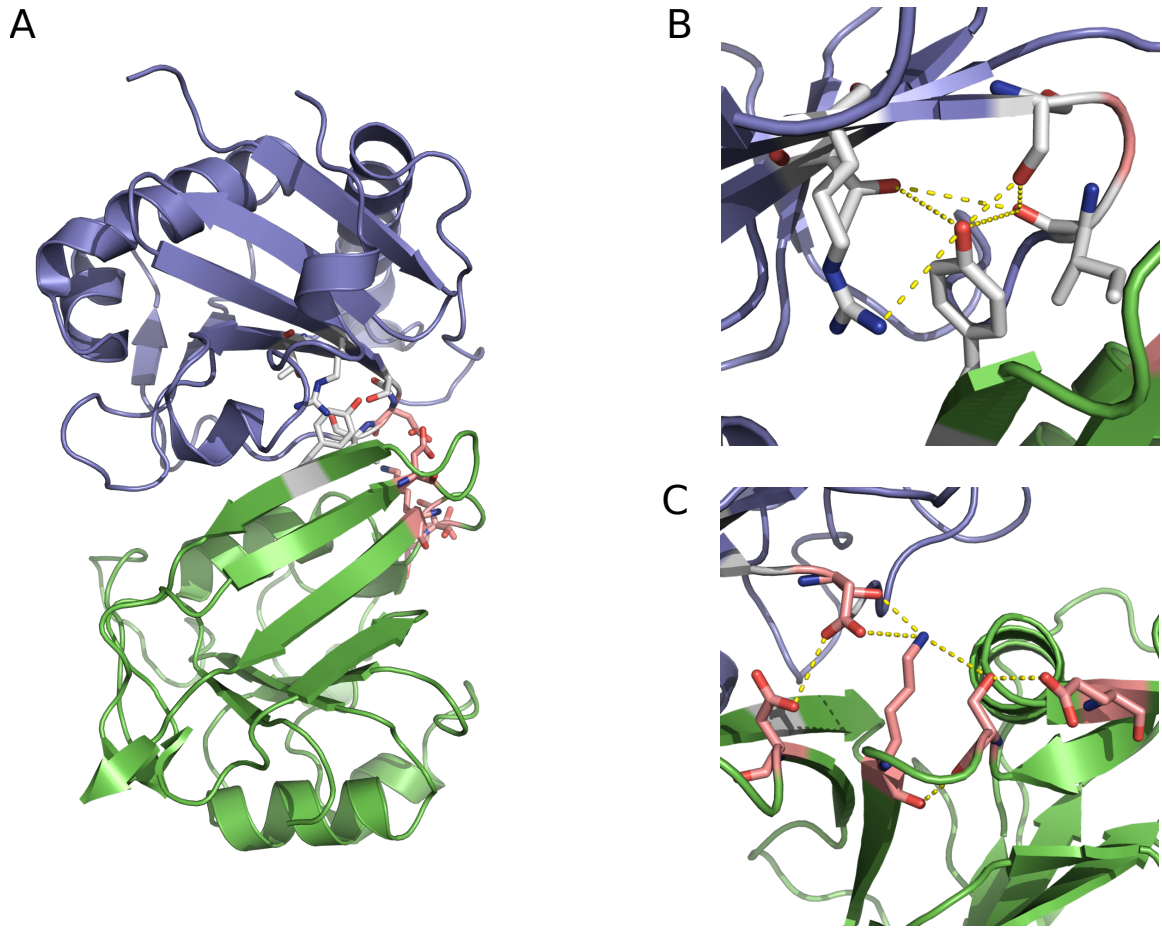


Figure 2: The two hydrogen bonding networks. GP1 is shown in blue and hTfR1 is shown in green. (A) The first network including Y211 and R111 is shown in white, and the second network containing N348 is shown in pink. (B) Near view of the first network with contacts in yellow. (C) Near view of the second network with contacts in yellow.

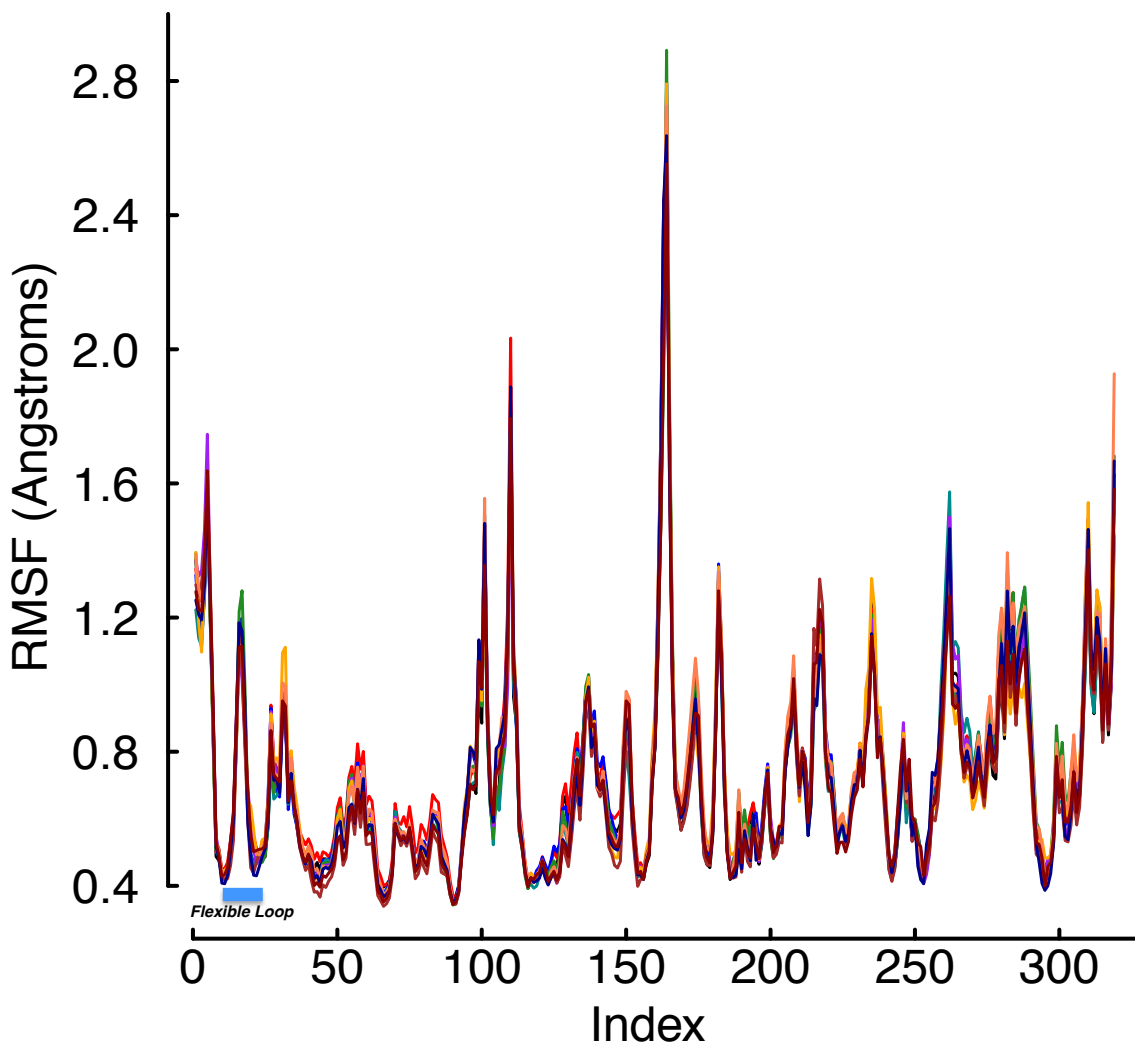


Figure 3: RMSF values during equilibration. The RMSF values for every site in the bound complex computed during the equilibration phase of the protocol. Each color represents the average over 20 trajectories of a single mutant. Indices 17-25 are the hTfR flexible loop. The plot shows the flexibility of each site is essentially independent of mutation, and two sites (indices 17 and 18) above 0.72 Å are a part of the flexible loop in the free receptor. However, these two residues are not actually found in the protein–protein interface, but rather are almost completely solvent exposed with the virus bound.

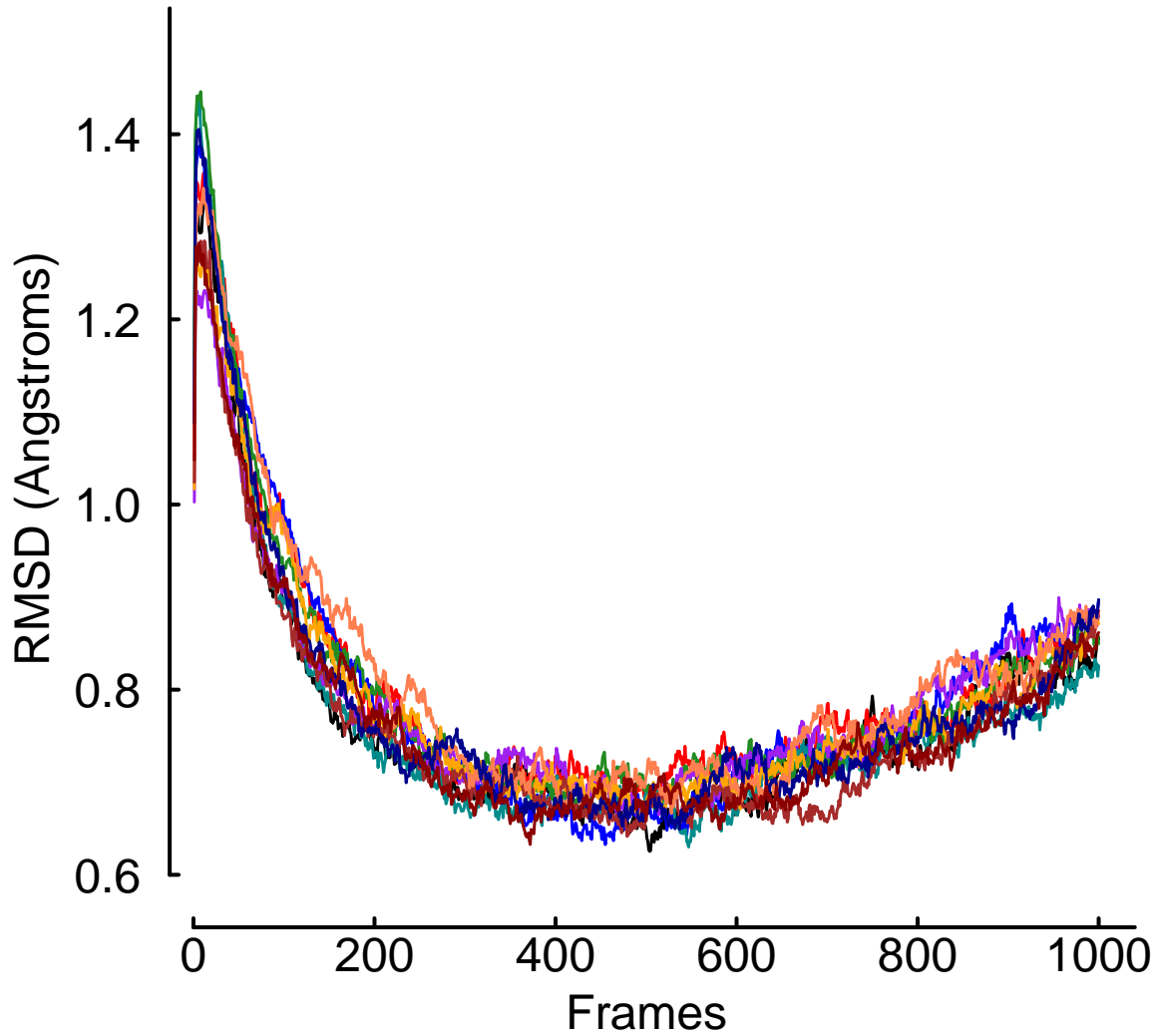


Figure 4: RMSD values during equilibration. The RMSD values over the time of the trajectory computed during the equilibration phase of the protocol. Each color represents the average over 20 trajectories of a single mutant. The plot shows none of the mutants causes immediate unbinding of the protein–protein complex. In addition, the universal upward trend near the end of the equilibration trajectories may indicate the crystal is more tightly packed than would normally occur in solution.

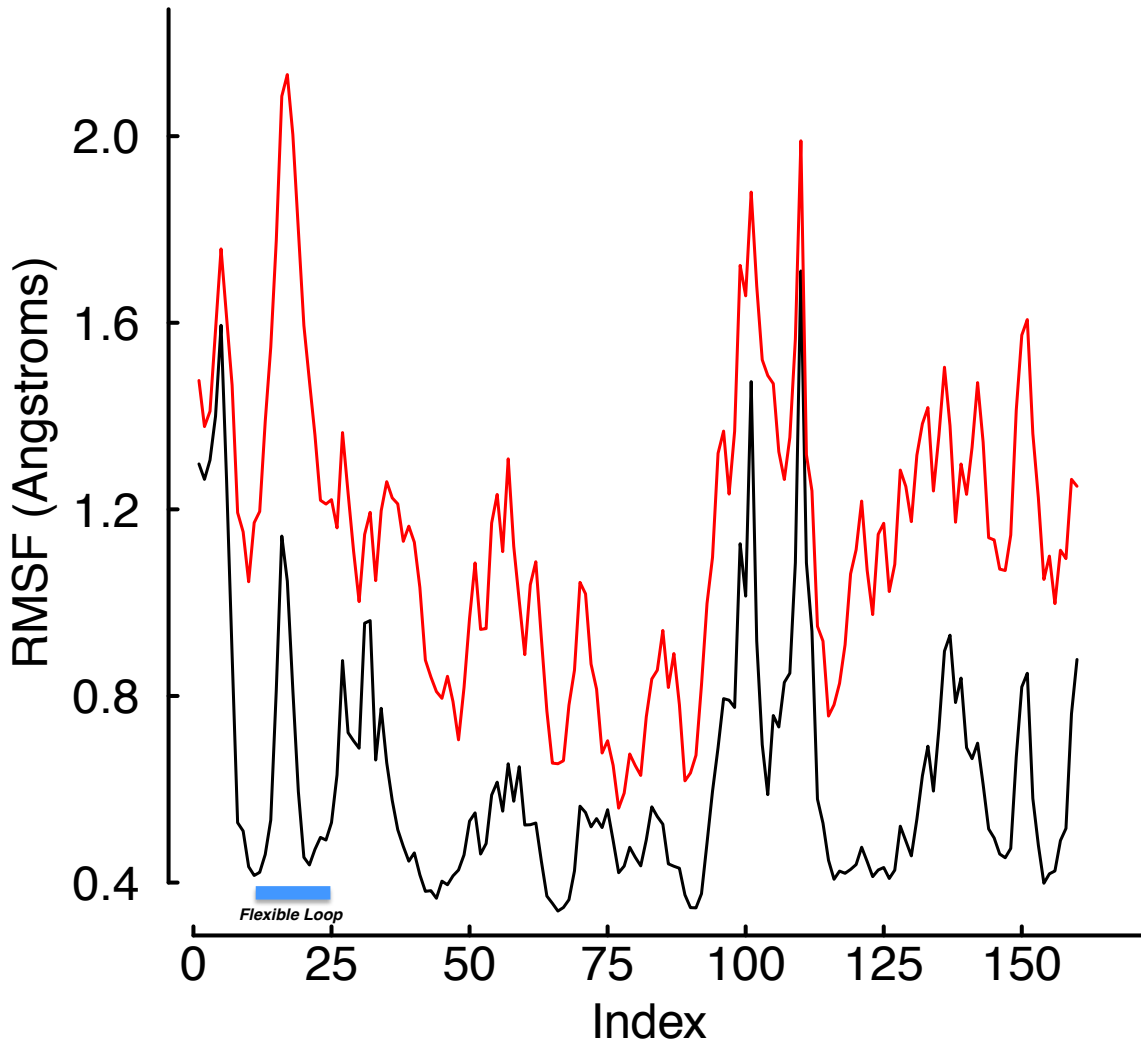


Figure 5: RMSF values of WT hTfR in equilibration and SMD. The RMSF values for every site in the WT receptor were computed during the equilibration phase and during final 50 frames of the SMD trajectories. The black line was computed over equilibration and the red line during SMD. The plot shows the solution mobility of the hTfR flexible loop increases more than the average during the unbinding process.

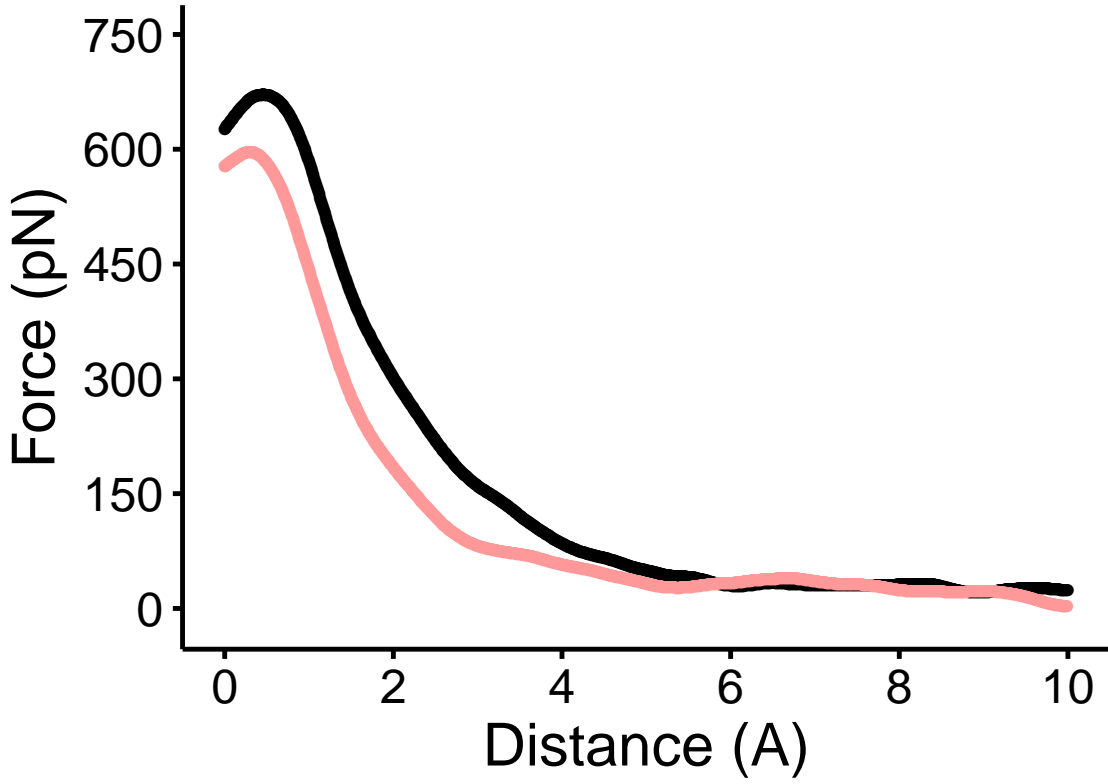


Figure 6: Force versus distance curve of WT and the Y211A mutant. The average force curve for 50 replicates of the WT complex is shown in black, and the average of 50 replicates of the Y211A mutant is shown in red. There is a large difference in both maximum applied force and AUC between the two complexes.

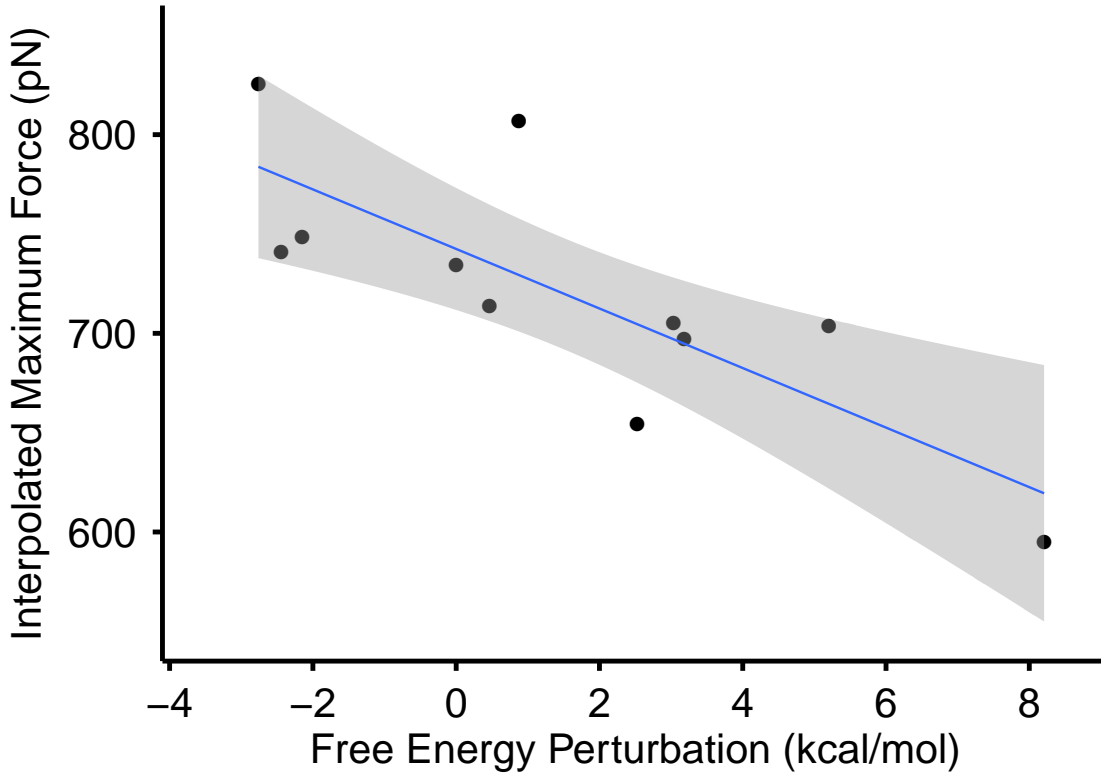


Figure 7: Max force versus free energy perturbation. Scatter plot of maximum force in SMD versus the relative free energy difference calculated by FEP for all 10 mutants tested plus the WT complex. The WT complex for FEP was simply set to 0.0. The correlation between the two is  $r = -0.795$  with  $p = 0.0034$ .

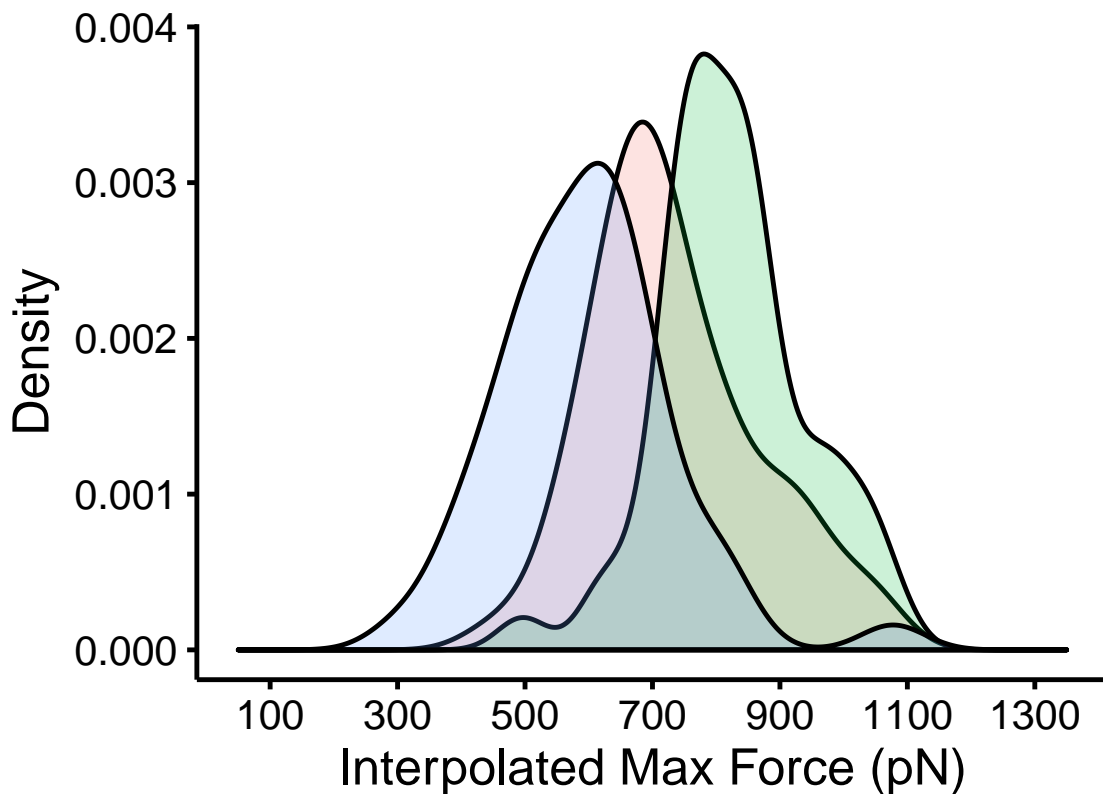


Figure 8: Distribution of interpolated maximum force for three different GP1/hTfR1 complexes. The WT GP1-hTfR1 complex in the middle is flanked by the tighter binding mutant Y211D on the right and the weaker binding double mutant N348W/Y211A on the left. The large non-overlapping areas indicate a large and statistically significant difference in these three complexes.

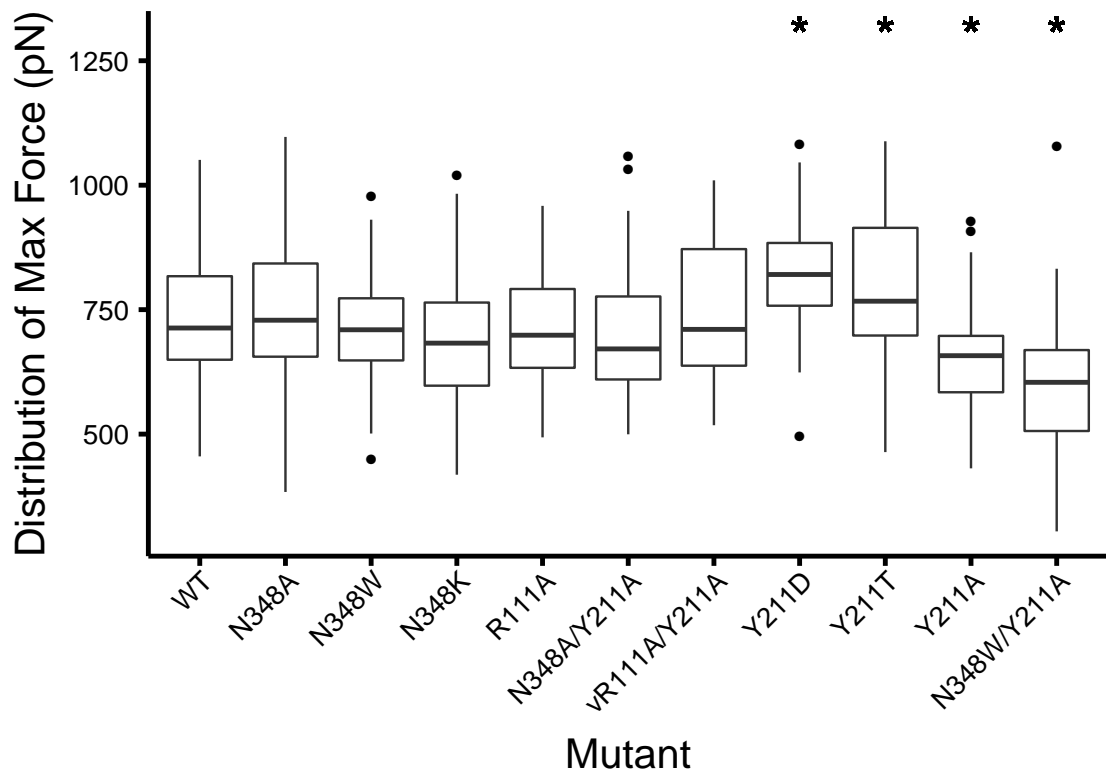


Figure 9: Distribution of interpolated maximum force for all bound complexes tested. Stars above the boxplots indicate a statistically significant difference in mean maximum force relative to the WT complex.

Table 1: Summary of prior information available for each mutation tested. Observed *in vivo* refers to mutations that have been observed in rodent populations. Phenotype *in vitro* refers to the observed phenotype in *in vitro* viral entry assays.

Mutation	Observed <i>in vivo</i>	Phenotype <i>in vitro</i>
WT	Yes	Normal Entry
N348A	No	-
N348K	Yes	Diminished Entry
N348W	No	-
vR111A	No	Diminished Entry
N348A/Y211A	No	-
vR111A/Y211A	No	-
Y211D	Yes	No Expression
Y211T	No	Diminished Entry
Y211A	No	No Expression
N348W/Y211A	No	-

Table 2: Summary statistics for each mutation tested.  $\mu_{\text{MAF}}$  is the mean in piconewtons and  $\sigma_{\text{MAF}}$  is the standard deviation of maximum applied force over all simulations.  $\mu_{\text{AUC}}$  is the mean and  $\sigma_{\text{AUC}}$  is the standard deviation of AUC over all simulations.  $\Delta G$  is the free energy difference in kcal/mol calculated via FEP by the dual topology paradigm.

Mutation	$\mu_{\text{MAF}}$ (pN)	$\sigma_{\text{MAF}}$	$\mu_{\text{AUC}}$	$\sigma_{\text{AUC}}$	$\Delta G$ (kcal/mol)
WT	734.4856	131.6513	145460.4	60232.26	0.000
N348A	748.5217	137.4864	133913.9	51078.64	-2.149
N348K	705.0707	108.5079	141084.4	54450.28	+3.184
N348W	697.3642	132.6436	136886.0	53796.44	+3.033
vR111A	713.8081	106.7374	136103.2	52070.85	+0.466
N348A/Y211A	703.7027	128.5866	113464.2	57451.62	+5.203
vR111A/Y211A	741.0642	131.6287	130070.6	47665.56	-2.440
Y211D	825.2586	115.4343	158878.7	63039.08	+2.760
Y211T	806.8593	136.5648	167110.7	78849.29	+0.875
Y211A	654.1138	108.5343	108090.0	43661.09	+2.526
N348W/Y211A	594.9044	134.8233	108984.2	45451.00	+8.206

Table 3: Pairwise differences (row variable minus column variable) in mean maximum applied force. Bolded values are statistically significant at  $p < 0.05$ .

	WT	N348A	N348W	N348K	vR111A	N348A/Y211A	vR111A/Y211A	Y211D	Y211T	Y211A
N348A	+14.036									
N348W	-29.414	-43.451								
N348K	-37.121	<b>-51.157</b>	-7.7060							
vR111A	-20.677	-34.713	+8.7370	+16.443						
N348A/Y211A	-30.782	-44.819	-1.3670	+6.3380	-10.105					
vR111A/Y211A	+6.5790	-7.4570	+35.993	+43.700	+27.256	+37.361				
Y211D	<b>+90.772</b>	<b>+76.736</b>	<b>+120.19</b>	<b>+127.89</b>	<b>+111.45</b>	<b>+121.56</b>	<b>+84.194</b>			
Y211T	<b>+72.373</b>	<b>+58.337</b>	<b>+101.79</b>	<b>+109.50</b>	<b>+93.051</b>	<b>+103.16</b>	<b>+65.795</b>	-18.399		
Y211A	<b>-80.371</b>	<b>-94.407</b>	-50.956	-43.250	<b>-59.694</b>	-49.588	<b>-86.950</b>	<b>-171.14</b>	<b>-152.75</b>	
N348W/Y211A	<b>-139.58</b>	<b>-153.62</b>	<b>-110.17</b>	<b>+102.46</b>	<b>-118.903</b>	<b>-108.80</b>	<b>+146.16</b>	<b>+230.35</b>	<b>-211.95</b>	<b>-59.209</b>

Table 4: Pairwise difference  $p$ -values for maximum applied force. Bolded values are statistically significant at  $p < 0.05$ .

	WT	N348A	N348W	N348K	vR111A	N348A/Y211A	vR111A/Y211A	Y211D	Y211T	Y211A
N348A	0.60									
N348W	0.31	<b>0.077</b>								
N348K	0.20	<b>0.038</b>	0.81							
vR111A	0.51	0.16	0.79	0.60						
N348A/Y211A	0.29	0.07	0.95	0.81	0.77					
vR111A/Y211A	0.82	0.79	0.21	0.13	0.35	0.20				
Y211D	<b>0.00093</b>	<b>0.0012</b>	<b>1.4x10<sup>-5</sup></b>	<b>5.0x10<sup>-6</sup></b>	<b>5.6x10<sup>-5</sup></b>	<b>1.2x10<sup>-5</sup></b>	<b>0.0022</b>			
Y211T	<b>0.01</b>	<b>0.018</b>	<b>0.00022</b>	<b>8.7x10<sup>-5</sup></b>	<b>0.0008</b>	<b>0.0002</b>	<b>0.021</b>	0.56		
Y211A	<b>0.0034</b>	<b>7.2x10<sup>-5</sup></b>	0.074	0.13	<b>0.035</b>	0.079	<b>0.0016</b>	<b>4.2x10<sup>-10</sup></b>	<b>4.2x10<sup>-8</sup></b>	
N348W/Y211A	<b>3.9x10<sup>-7</sup></b>	<b>1.1x10<sup>-10</sup></b>	<b>6.5x10<sup>-5</sup></b>	<b>0.00021</b>	<b>1.6x10<sup>-5</sup></b>	<b>7.2x10<sup>-5</sup></b>	<b>1.3x10<sup>-7</sup></b>	<b>1.2x10<sup>-16</sup></b>	<b>2.0x10<sup>-14</sup></b>	<b>0.036</b>

Table 5: Pairwise difference  $p$ -values for interpolated AUC. Bolded values are statistically significant at  $p < 0.05$ .

	WT	N348A	N348W	N348K	vR111A	N348A/Y211A	vR111A/Y211A	Y211D	Y211T	Y211A
N348A	0.33									
N348W	0.76	<b>0.59</b>								
N348K	0.59	0.80	0.76							
vR111A	0.55	0.85	0.76	0.94						
N348A/Y211A	<b>0.017</b>	0.07	<b>0.031</b>	0.076	0.08					
vR111A/Y211A	0.26	0.76	0.46	0.68	0.72	0.22				
Y211D	0.33	<b>0.029</b>	0.18	0.09	0.08	<b>0.00046</b>	<b>0.029</b>			
Y211T	0.09	<b>0.0056</b>	<b>0.046</b>	<b>0.027</b>	<b>0.023</b>	<b>4.1x10<sup>-5</sup></b>	<b>0.006</b>	0.59		
Y211A	<b>0.0056</b>	<b>0.027</b>	<b>0.016</b>	<b>0.029</b>	<b>0.031</b>	0.75	0.09	<b>8.2x10<sup>-5</sup></b>	<b>8.5x10<sup>-6</sup></b>	
N348W/Y211A	<b>0.006</b>	<b>0.029</b>	<b>0.017</b>	<b>0.032</b>	<b>0.034</b>	0.76	0.1	<b>9.4x10<sup>-5</sup></b>	<b>8.5x10<sup>-6</sup></b>	0.94